

Structure and Interface Analysis of Diamond on an AlGaN/GaN HEMT Utilizing an in Situ SiNx Interlayer Grown by MOCVD

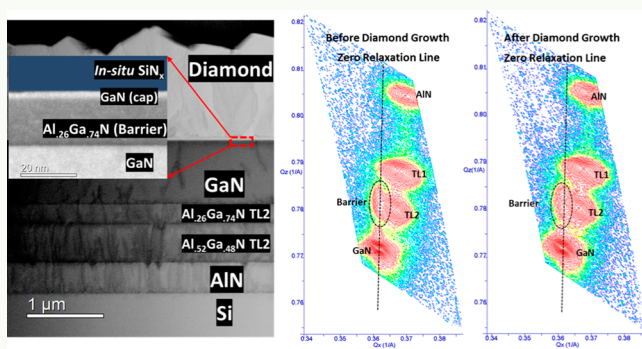
Anwar Siddique,[†] Raju Ahmed,^{†,ID} Jonathan Anderson,[†] Mohammad Nazari,[§] Luke Yates,[‡] Samuel Graham,^{‡,ID} Mark Holtz,^{†,§,ID} and Edwin L. Piner*,^{†,§,ID}

[†]Materials Science, Engineering and Commercialization Program and [§]Department of Physics, Texas State University, San Marcos, Texas 78666, United States

[‡]George W. Woodruff School of Mechanical Engineering and Heat Lab, Georgia Institute of Technology, Atlanta, Georgia 30332, United States

ABSTRACT: Integration of diamond and AlGaN/GaN high-electron mobility transistors (HEMTs) terminated with an in situ grown SiN_x interface layer via metal organic chemical vapor deposition is investigated. The effect of diamond growth on the structure and interface properties of the HEMT is studied using high-resolution X-ray diffraction, micro-Raman spectroscopy, atomic force microscopy, and scanning transmission electron microscopy (STEM). No structural or physical damage is observed to the HEMT device layers as a result of the hot filament chemical vapor deposition diamond fabrication process. The TEM cross section confirms the smooth and abrupt interface of in situ SiN_x/AlGaN/GaN before and after the diamond growth, with no detectable carbon diffusion into the GaN buffer layer. However, selective degradation of the in situ SiN_x dielectric adhesion layer was observed at the SiN_x/diamond interface. Using time domain thermoreflectance (TDTR), the effective isotropic thermal conductivity of the diamond was determined to be 176_{-35}^{+40} W/m·K. The effective thermal boundary resistance of the diamond/GaN interface (including the SiN_x and additional layers) was $52.8_{-3.2}^{+5.1}$ m²·K/GW.

KEYWORDS: GaN, AlGaN/GaN HEMT, CVD diamond, HRXRD, RSM, biaxial stress, TBR



1. INTRODUCTION

III-Nitride-based high-electron mobility transistor (HEMT) devices possess wide bandwidth and high breakdown voltage because of their high electron velocity, high-density two-dimensional electron gas (2DEG), and large breakdown field. The maximum radiofrequency (RF) power density for GaN-based HEMTs reported to date is 41.4 W mm^{-1} at 4 GHz.¹ More recently, AlGaN/GaN-based transistors for terahertz (THz) emitters and detectors have been reported that can operate from 0.75 to 2.1 THz.^{2,3} Furthermore, AlGaN/GaN HEMTs grown on silicon are reported to have a switching speed as high as ~ 150 GHz⁴ while the power densities can exceed 12 W/mm^2 as well as under harsh operational conditions.⁶

In a GaN-based heterojunction device, a 2DEG is induced at the AlGaN/GaN interface without doping. This is due to large spontaneous and piezoelectric polarization effects as well as the band offset between GaN and AlGaN.⁷ For GaN-based HEMTs, the high current driven through the channel is confined to the very narrow, <10 nm, 2DEG and therefore produces significant self-heating (as high as 350°C for GaN on Si) in the active region of the device.⁸ Because the 2DEG and the active GaN/AlGaN layers are very thin, the dissipation of heat from the self-heating source is predominantly vertical.⁸

Therefore, a low-resistance thermal pathway from the self-heating source to a nearest heat sink (e.g., a high thermally conductive substrate) is highly desired.

Owing to its outstanding bulk thermal conductivity, which can exceed $2000 \text{ W/m}\cdot\text{K}$,⁹ a chemical vapor deposition (CVD) polycrystalline diamond is the superior choice as a heat spreading material, especially when compared with standard GaN-based substrates such as Si, 6H-SiC, and Al₂O₃. Altman et al. used diamond as a substrate to show a $2.7\times$ reduction in the thermal resistivity and a $3\times$ increase in device areal density compared to GaN-on-SiC devices.¹⁰ To achieve the maximum benefit of diamond heat spreading, the diamond thin film must be in direct contact with the HEMT stack and most preferably to the topmost AlGaN barrier layer nearest the device active region.

Inclusion of a diamond heat spreader with the AlGaN/GaN HEMT can be realized in different ways. One approach is to replace the original III-nitride growth substrate by wafer bonding of a diamond substrate to the AlGaN/GaN HEMT. A second approach is direct growth of diamond on the back

Received: March 1, 2019

Accepted: July 8, 2019

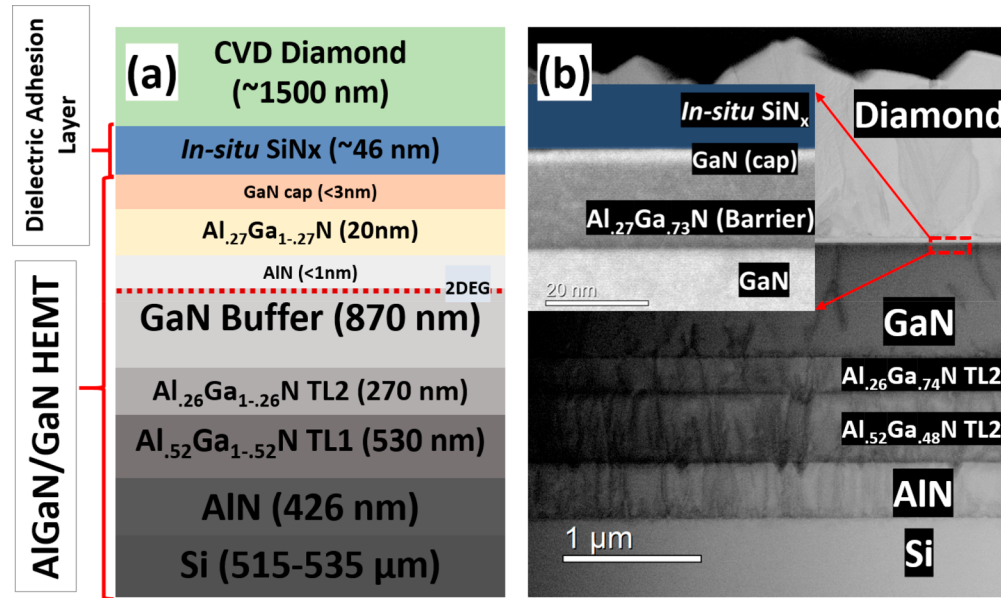


Figure 1. (a) Schematic of the target diamond-on-AlGaN/GaN HEMT structure using MOCVD grown *in situ* SiN_x as the dielectric adhesion layer (not drawn to the scale), and (b) bright-field STEM images of the structure after diamond growth. Inset indicates the *in situ* SiN_x/GaN(cap)/AlGaN(barrier)/GaN interface region, post-diamond growth.

(GaN) side of the wafer.^{11–13} In both approaches, additional processing steps are required, such as transfer to a handle wafer, substrate removal, wafer bonding, and/or handle wafer removal. The electrical, chemical, and thermal properties (thermal conductivity of diamond and thermal boundary resistance)^{10,12} of the GaN–diamond interfaces have been extensively studied with these approaches.

A third approach to achieve the desired diamond integration is directly growing the CVD diamond layer on the epi-side (top AlGaN surface) of the passivated active layer.^{14–22} Challenges to diamond-on-AlGaN/GaN growth include degradation of III-nitride layers in the harsh CVD environment²³ and thermal stresses due to the mismatch of the materials' thermal expansion coefficients.²⁴ Any change in the stress–strain state in AlGaN/GaN heterostructures, especially in the fully strained pseudomorphically grown AlGaN barrier layer, would have a significant impact on the 2DEG characteristics.⁷ Wang et al.²² has reported on the overall impact of stress due to high-temperature CVD diamond integration with a dielectric adhesion layer through simulation (thermal stress on GaN, SiN_x, and diamond) and Raman measurements (bulk GaN). However, strain in the pseudomorphically grown AlGaN barrier layer is impacted differently than that of bulk GaN. Therefore, for a proper understanding of the impact of the CVD diamond integration-induced stress–strain state on the 2DEG characteristics, the barrier layer stress must be evaluated but cannot be done using Wang et al.'s Raman approach. Using direct diamond growth, a 25% improvement in breakdown voltage²⁵ and a 20% lower channel temperature at equivalent power dissipation have been reported.²¹ Zhou et al. predicted that a 15% reduction in self-heating for devices based on similar material stacks can be realized with CVD diamond grown on the HEMT structure.¹⁸ Although the potential effectiveness of this approach is very promising, detailed studies of the diamond–AlGaN/GaN interface properties as well as the impact of the diamond growth on the III-nitride materials, requires further investigation.

In this study, we report *in situ* SiN_x grown by metal organic chemical vapor deposition (MOCVD) immediately following the AlGaN/GaN HEMT growth. Subsequently, CVD diamond deposition is conducted in a hot filament CVD growth system. We evaluated the impact on the material properties (stress/strain state) of the III-nitride layers before and after diamond growth by high-resolution X-ray diffraction (HRXRD)-based reciprocal space mapping (RSM) and from visible and ultraviolet (UV) micro-Raman measurements. HRXRD RSM around the III-nitride (10–14) asymmetric peaks is used to determine the in-plane AlGaN barrier layer strain and is a more accurate stress–strain measurement of the AlGaN/GaN heterostructure than characterization by Raman (which cannot resolve the AlGaN barrier layer separately from the GaN buffer). Scanning transmission electron microscopy (STEM) imaging was performed to evaluate the structural and elemental properties of the *in situ* SiN_x passivated AlGaN/GaN HEMT interface before and after the diamond growth. Finally, time domain thermoreflectance (TDTR) was performed to evaluate the thermal conductivity of the CVD diamond and the effective thermal boundary resistance (TBR) of the diamond/GaN interface.

2. EXPERIMENTAL DETAILS

The AlGaN/GaN HEMT structure was grown on a low-resistivity (40 Ω·cm) Si(111) substrate using a custom-built MOCVD reactor.²⁶ Figure 1(a) shows a schematic diagram of the target diamond-on-AlGaN/GaN HEMT structure. The III-nitride layers were grown at 1020 °C using a chamber pressure ranging from 30 to 100 Torr, while the V/III ratio was varied from 900 to 1700. Source materials include trimethylgallium, trimethylaluminum, ammonia, and silane (2% SiH₄ in hydrogen) with H₂ as the carrier gas. Growth was initiated using AlN as the nucleation layer on Si. Subsequent step-graded Al_xGa_{1-x}N transition layers with $x = 0.52$ for transition layer 1 (TL1) and $x = 0.26$ for transition layer 2 (TL2) were grown to compensate for thermal expansion mismatch and lattice mismatch. An 870 nm thick unintentionally doped GaN buffer layer was grown on the transition layers. A 1.5 nm AlN profile layer was then grown followed by a pseudomorphically strained 20 nm barrier layer (Al_{0.27}Ga_{0.73}N).

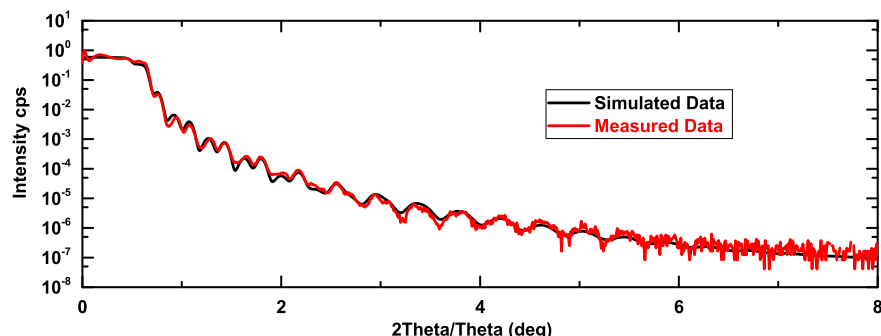


Figure 2. Measured and simulated grazing incidence X-ray reflectivity of the in situ SiN_x passivated III-nitride HEMT heterostructure.

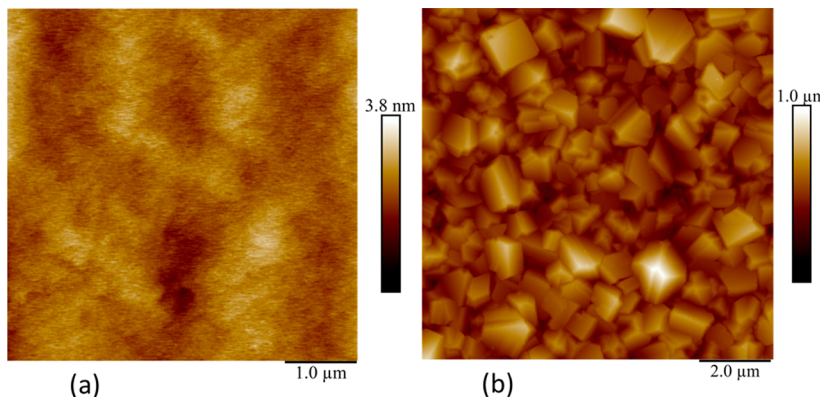


Figure 3. AFM images of (a) 5 by 5 μm in situ SiN_x surface and a (b) 10 by 10 μm diamond surface confirming the smooth, continuous in situ SiN_x surface and fully coalesced diamond surface.

Finally, a \sim 1.5 nm GaN cap was grown to complete the baseline reference AlGaN/GaN HEMT. For the experimental wafer, SiH_4 was then introduced to the chamber, while the same temperature and chamber pressure (100 Torr) of the GaN cap layer were maintained to produce the \sim 46 nm thick in situ SiN_x .

For the diamond CVD process, nanodiamond seeds were dispersed using a photoresist-based spin coating technique as reported by Ahmed et al.²⁷ A power of 6 kW was driven through an array of nine tungsten wires of 0.01" diameter, which resulted in a 2200 $^{\circ}\text{C}$ wire filament temperature. The rotating substrate was positioned 6 mm from the tungsten wire array to produce a substrate temperature of 720–750 $^{\circ}\text{C}$ and a uniform diamond growth rate. Growth was carried out for 7 h using 60 sccm of methane and 3 sccm of oxygen with 2000 sccm of hydrogen into the hot filament CVD (HFCVD) chamber, while a pressure of 20.8 Torr was maintained. As discussed below, this process resulted in a $1.46 \pm 0.10 \mu\text{m}$ thick fully coalesced diamond and uniform coverage across the wafer.

X-ray reflectometry (XRR) of the in situ SiN_x was performed using a Bruker SmartLab 3 kW system to determine the initial thickness and density of the MOCVD grown SiN_x dielectric adhesion layer. Using a two-bounce Ge (2 2 0) monochromator, HRXRD reciprocal space mapping (RSM) was performed around both the GaN asymmetric (1 0 $\bar{1}$ 4) and symmetric (0 0 2) planes to determine the stress and composition of the constituent layers before and after diamond deposition. A Bruker Dimension ICON system was used in tapping mode for atomic force microscopy (AFM) measurements of the in situ SiN_x surface before diamond growth and of the diamond surface after growth to evaluate roughness and grain size. Visible (532 nm) and UV (363.8 nm) micro-Raman measurements were performed to evaluate the structural and interface properties of III-nitride layers and to ascertain the effects on the GaN before and after diamond growth.²⁸ Bulk samples were used to determine the GaN (TDI, Inc.) and AlN (Crystal IS) reference phonon energies. Further details of the measurement can be found elsewhere.^{24,26}

Scanning transmission electron microscopy (STEM) was used to analyze the interface characteristics and layer thicknesses before and after diamond deposition. Cross-sectional samples were prepared using standard focused ion beam (FIB) techniques using a FEI Helios Nanolab 400 DualBeam system by first depositing a protective Pt layer and milling using a 30 kV accelerating voltage. A final polishing step was then performed with an accelerating voltage of 2 kV to remove surface damage. Bright-field and high-angle annular dark-field (HAADF) images of the samples, as well as electron energy loss spectroscopy (EELS), were collected using a JEOL ARM 200F operating at 200 kV.

Finally, time domain thermoreflectance (TDTR) measurements²⁹ were performed to evaluate the diamond/GaN thermal boundary resistance (TBR) and the thermal conductivity of the polycrystalline diamond. To perform the TDTR, a 96 nm layer of Al was deposited by e-beam evaporation at room temperature.

3. RESULTS AND DISCUSSION

Figure 2 shows specular X-ray reflection from the SiN_x /GaN(cap)/AlGaN(barrier)/AlN(profile)/GaN layered structure, prior to diamond growth. The data exhibit well-defined periodic Kiessing fringes and are modeled using the layer thickness, interface roughness, and material density of each layer as parameters (Rigaku GlobalFit, which incorporates both optimization and least-squares refinement.) The layer thicknesses were determined to be 45.9 ± 0.1 nm for SiN_x , 0.5 ± 0.1 nm for the GaN cap, and 20.4 ± 0.1 nm for the AlGaN barrier.

The SiN_x density obtained from the model, $3.47 \text{ g}\cdot\text{cm}^{-3}$, is higher than that of plasma enhanced chemical vapor deposition (PECVD) SiN_x ($2.0\text{--}2.8 \text{ g}\cdot\text{cm}^{-3}$) as reported by Huang et al.³⁰ and low-pressure chemical vapor deposition (LPCVD) SiN_x ($2.9\text{--}3.1 \text{ g}\cdot\text{cm}^{-3}$) reported by Stoffel et al.³¹ while comparable

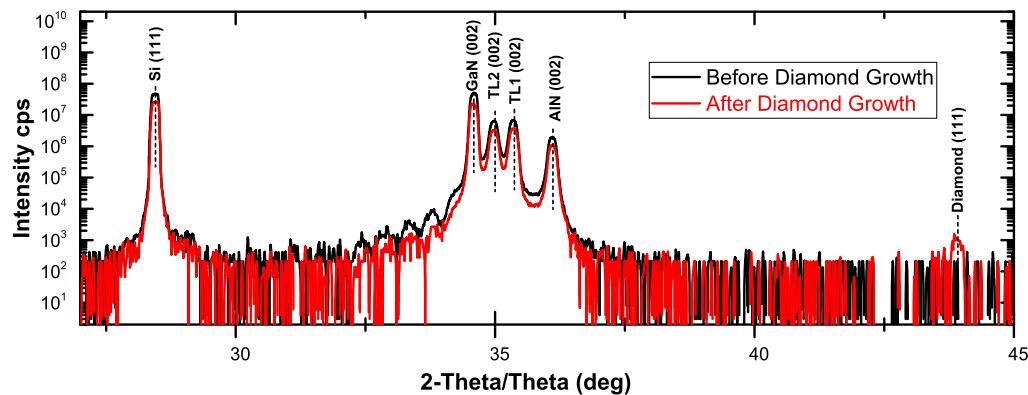


Figure 4. HRXRD 2-theta/theta spectrum of the AlGaN/GaN structure on Si (111) before and after diamond growth.

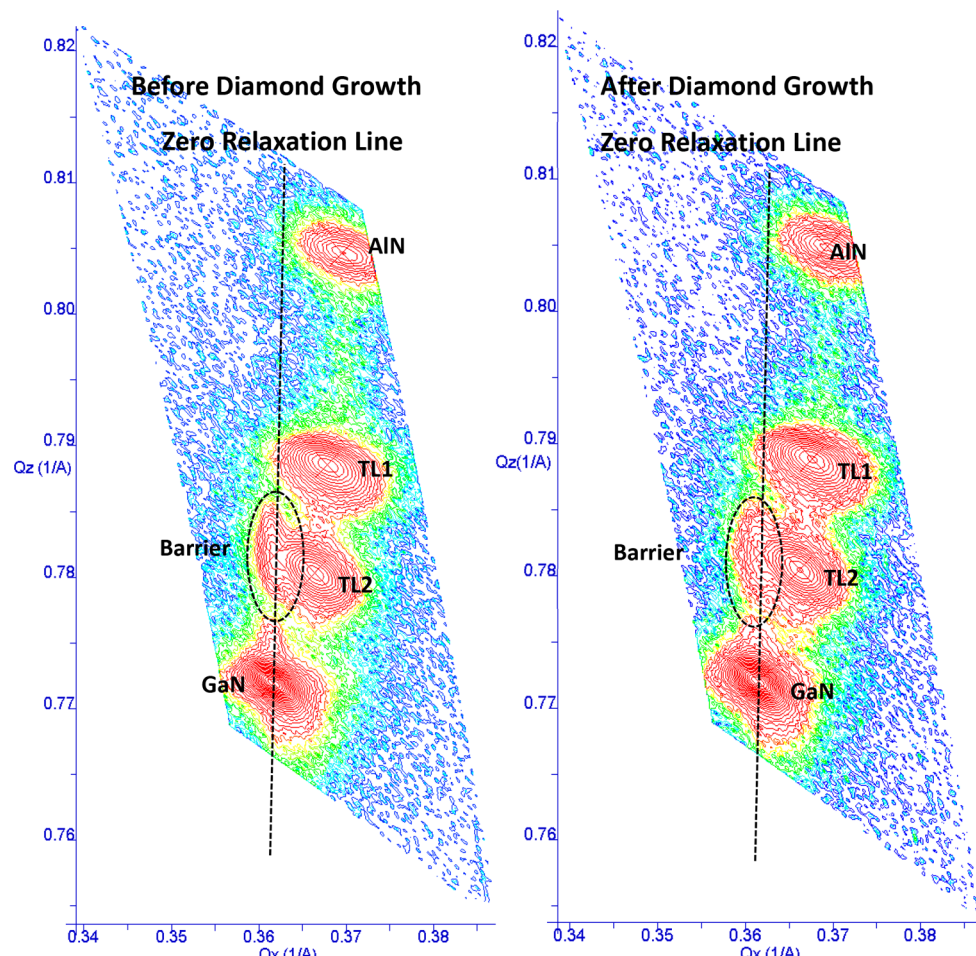


Figure 5. RSM contour plots of the AlGaN/GaN HEMT wafers with AlN, GaN, TL1 ($\text{Al}_{0.51}\text{Ga}_{0.49}\text{N}$), TL2 ($\text{Al}_{0.26}\text{Ga}_{0.74}\text{N}$), and barrier layer ($\text{Al}_{0.27}\text{Ga}_{0.73}\text{N}$) reflections collected around their asymmetric (10–14) planes. The dotted line indicates the zero-relaxation line along the crystallographic a -axis. The dotted ellipses highlight the strained barrier layer peaks. The axes are converted to Q_z and Q_x reciprocal coordinates ($Q_z = 1/d_z$; $Q_x = 1/d_x$). The color scheme shows the variation in intensity of the diffracted beam, with red representing the highest diffraction intensity and blue representing the lowest.

to MOCVD SiN_x ($3.6\text{--}3.8 \text{ g}\cdot\text{cm}^{-3}$) reported by Gamarra et al.³² The derived growth rate for the in situ MOCVD SiN_x was $\sim 2 \text{ nm}/\text{min}$. From XPS surface stoichiometric analysis, $x = [\text{N}]/[\text{Si}]$ for this SiN_x layer was found to be 1.13.

Figure 3(a) shows a 5 by 5 μm AFM image of the in situ SiN_x surface before diamond deposition. A very smooth surface morphology is obtained with an RMS roughness (R_q) of 0.43 nm. Figure 3(b) shows a 10 by 10 μm AFM image of

the diamond surface after 7 h of growth. Coalesced diamond coverage is confirmed. The RMS surface roughness is 92.4 nm, while the average grain size and distribution calculated by the linear intercept method was $0.73 \pm 0.32 \mu\text{m}$ for this $1.25^{+0.12}_{-0.12} \mu\text{m}$ thick diamond film (measured from STEM data).

3.1. HRXRD Results. HRXRD measurements were used to determine whether the underlying III-nitride layers have been protected during 7 h of diamond growth in the HFCVD

Table 1. Relaxed Lattice Parameters for AlN and GaN and Corresponding Elastic Constants³⁷

	a_0	c_0	C_{13}	C_{33}	C_{11}	C_{12}	Poisson's ratio
GaN	3.189	5.186	106 ± 20	398 ± 20	390 ± 15	145 ± 20	0.210
AlN	3.112	4.982	108 ± 5	373 ± 10	396 ± 10	137 ± 10	0.224

environment. HRXRD 2-theta/theta scans in Figure 4 show the diffraction patterns before and after diamond growth. The III-nitride (GaN, AlN, TL1, and TL2) second-order (0002) diffraction peaks are present and have not substantially changed before and after diamond growth. This confirms that the III-nitride layers beneath the AlGaN barrier layer are fully protected by the in situ SiN_x passivation layer during diamond CVD. Following diamond growth, the corresponding diamond (1 1 1) diffraction peak is present at 43.90° . The fwhm values of the GaN (0002) ω -scan, before and after growth, are 587 ± 1 and 598 ± 1 arcsec, respectively. This 2% increase, post-diamond growth compared to pre-growth, is consistent with similar in situ SiN_x passivated HEMT structures (600 arcsec) grown by MOCVD as reported by Germain et al.³³

Because the strained barrier layer ($\text{Al}_{0.27}\text{Ga}_{0.73}\text{N}$) has a similar composition as TL2 ($\text{Al}_{0.26}\text{Ga}_{0.74}\text{N}$), the symmetric (0002) HRXRD scan cannot independently resolve the barrier layer, as the two layers have nearly identical interplanar spacings along the c -axis. Therefore, RSM around the asymmetric (10–14) plane was performed to analyze the strained AlGaN barrier layer. Because the thin (20 nm) AlGaN barrier layer can be independently measured, the effectiveness of the SiN_x adhesion layer for protecting the barrier layer during diamond growth can be accurately ascertained. Figure 5 presents the HRXRD RSM data before (a) and after (b) diamond deposition. The XRD goniometer was first normalized to the GaN (10–14) peak. The measurements were performed using grazing exit (GE) geometry to minimize instrument-induced aberration. The data are presented in a contour representation of diffraction intensity in reciprocal space coordinates $Q_{(hkl)z}$ and $Q_{(hkl)x}$. Peak positions in this coordinate system are readily converted into interplanar spacing (d_z , d_x) and, hence, the lattice constants (c , a). The vertical dotted line in each panel represents the zero-relaxation line across the GaN a -axis. For an AlGaN barrier layer grown pseudomorphically on GaN, the barrier layer peak (within the dotted ellipse) lies on the zero-relaxation line. The diffraction peaks from the AlN, TL1, and TL2 layers lie on the right side of the zero-relaxation line corresponding to partially or fully relaxed material.

The reciprocal lattice vector $Q_{(hkl)}$ for a given hkl plane is defined in terms of interplanar spacing d_{hkl} and lattice parameters, a and c in the wurtzite crystal structure. These relationships are described in the literature^{34,35} so that HRXRD measurements can be used to determine strain in the III-nitride layers. The resulting in-plane ($\varepsilon_{xx} = (a - a_0)/a_0$) and out-of-plane ($\varepsilon_{zz} = (c - c_0)/c_0$) strains are related according to $\varepsilon_{zz} = -\frac{2\nu}{1-\nu}\varepsilon_{xx} = -\left(\frac{2C_{13}}{C_{33}}\right) \times \varepsilon_{xx}$ where the

Poisson ratio is $\nu = \frac{C_{13}}{C_{13} + C_{33}}$.

For unstrained $\text{Al}_x\text{Ga}_{1-x}\text{N}$ layers, such as TL1 and TL2, a single diffraction measurement (e.g., c lattice constant) and Vegard's Law³⁶ are sufficient for determining the AlN composition (x). For partially relaxed or fully strained layers, such as the pseudomorphic AlGaN barrier layer, both a and c

lattice constants are needed to calculate the $\text{Al}_x\text{Ga}_{1-x}\text{N}$ composition ($x = \text{Al}\%$).

For a fully strained $\text{Al}_x\text{Ga}_{(1-x)}\text{N}$ layer, where x is unknown, and using Vegard's Law to express the relaxed alloy lattice parameters and elastic constants (C_{ij}), the in-plane and out-of-plane strain relation can be rewritten as^{35,34}

$$\frac{c_m(x) - [xc_0^{\text{AlN}} + (1-x)c_0^{\text{GaN}}]}{[xc_0^{\text{AlN}} + (1-x)c_0^{\text{GaN}}]} = -\frac{2[xC_{13}^{\text{AlN}} + (1-x)C_{13}^{\text{GaN}}]}{[xC_{33}^{\text{AlN}} + (1-x)C_{33}^{\text{GaN}}]} \times \frac{a_m(x) - [xa_0^{\text{AlN}} + (1-x)a_0^{\text{GaN}}]}{[xa_0^{\text{AlN}} + (1-x)a_0^{\text{GaN}}]} \quad (1)$$

where subscript m denotes the measured lattice parameters. The relaxed lattice parameters and elastic constants used herein were reported by Vurgaftman et al.³⁷ and are presented in Table 1.

By considering x as a rational fraction, the above equations reduce to a simple third-order polynomial

$$Ax^3 + Bx^2 + Cx + D = 0 \quad (2)$$

where A , B , C , and D are the constant coefficients.

The measured lattice parameters $c_m(x)$ were determined from RSM around the GaN (0002) reflection, and lattice parameters $a_m(x)$ were determined from RSM around the GaN (10–14) reflection (see Figure 5). By solving eq 2, the AlN mole fraction for the fully strained AlGaN barrier layer was determined to be $x = 27\%$. By determining the exact x value for the strained barrier layer, ε_{xx} and ε_{zz} were determined and are presented in Table 2. Strain in III-nitride layers may be composed of hydrostatic (ε_h) and biaxial (ε_{ii}^b) components,^{34,38,39} where i represents direction x or z . As a result of the significantly different covalent radii of the Ga and the N atoms, GaN is prone to native defect formation.³⁸ It is well-known that GaN/Si grown using MOCVD contains a significant concentration of point defects, which can affect the lattice parameters through local expansion or contraction (depending on the density and types of point defects), thereby causing hydrostatic strain in the crystal.^{40,41} The hydrostatic strain can be quantified using $\varepsilon_h = \frac{\Delta c}{c_0} = \frac{\Delta a}{a_0} = bC$, where b is an expansion (contraction) factor for an individual defect, and C is their concentration.³⁸ For heterostructure epitaxial growth (e.g., AlGaN/GaN on Si or diamond on GaN), biaxial strain is induced in the Al(Ga)N layers because of lattice mismatch between the layers and different thermal expansion coefficients (CTE).^{35,38,40} Therefore, to better understand the true nature of the strain and the material quality before and after diamond growth, these strain components are considered. Uniaxial in-plane and out-of-plane strain can be expressed as a linear combination of biaxial strains (ε_{zz}^b , ε_{xx}^b), along c and a directions, respectively, and hydrostatic strain ε_h can be expressed as follows^{38,40}

$$\varepsilon_{zz} = \varepsilon_{zz}^b + \varepsilon_h \quad (3)$$

$$\varepsilon_{xx} = \varepsilon_{xx}^b + \varepsilon_h \quad (4)$$

Table 2. Measured Lattice Parameters along Both the *a*- and *c*-Axes, Calculated Uniaxial Strain, and Hydrostatic and Biaxial Stress from the Measured Lattice Parameters, before and after Diamond Growth

	before diamond growth										after diamond growth									
	measured lattice constant (Å)		measured strain (%)		hydrostatic strain (%)		biaxial strain (%)		biaxial stress (GPa)		measured lattice constant (Å)		measured strain (%)		hydrostatic strain (%)		biaxial strain (%)		biaxial stress (GPa)	
	<i>a</i>	<i>c</i>	ε_{xx}	ε_{zz}	ε_h	ε_{xx}^b	ε_{zz}^b	σ_{bs}	ε_{xx}	ε_{zz}	<i>a</i>	<i>c</i>	ε_{xx}	ε_{zz}	ε_h	ε_{xx}^b	ε_{zz}^b	σ_{bs}		
barrier	3.1911	5.1178	0.769	-0.265	0.099	0.669	-0.365	3.16	3.1913	5.1178	0.712	-0.288	0.064	0.648	-0.352	0.151	-0.080	0.72	3.06	
GaN	3.1926	5.1827	0.115	-0.071	-0.006	0.121	-0.065	0.58	3.1932	5.1813	0.133	-0.098	-0.018	0.008	0.326	-0.189	1.53			
AlN	3.1232	4.9720	0.327	-0.201	0.007	0.334	-0.193	1.57	3.1229	4.9709	0.350	-0.198								

Considering both biaxial and hydrostatic contributions, the strain relation can be rewritten as follows³⁸

$$\varepsilon_{zz} = \frac{c - (c_0 - \Delta c)}{c_0 - \Delta c} \quad (5)$$

, and

$$\varepsilon_{xx} = \frac{a - (a_0 - \Delta a)}{a_0 - \Delta a} \quad (6)$$

From the strain relation and rearranging the above equation, the hydrostatic strain can be expressed in terms of uniaxial strain and Poisson's ratio by the following expression

$$\varepsilon_h = \frac{1 - \nu}{1 + \nu} \left(\varepsilon_{zz} + \frac{2\nu}{1 - \nu} \varepsilon_{xx} \right) \quad (7)$$

Using the lattice parameters and elastic constants shown in Table 1, the strains are evaluated before and after diamond growth and are tabulated in Table 2. The corresponding in-plane biaxial stress σ_{bs} in the III-nitride layers can be expressed in terms of biaxial strain and biaxial elastic modulus,

$$M_f = C_{11} + C_{12} - 2 \frac{C_{13}^2}{C_{33}} \quad (8)$$

$$\sigma_{bs} = M_f \varepsilon_{xx}^b$$

Here C_{ij} represents the elastic constants of the corresponding III-nitride layers. With the lattice parameters and elastic constant from Table 1, biaxial stresses in the AlN and GaN layers are determined. Vegard's law is employed for the barrier material using the AlN mole fraction ($x = 27\%$) discussed earlier. Biaxial stresses for GaN, AlN, and the strained barrier layer, using eq 8 are included in Table 2. Measured uniaxial lattice strain ε_{xx} in the pseudomorphic barrier layer is +0.769% (tensile). The strain in the GaN, AlN, and barrier layers was in reasonable agreement with published reports.^{34,35} The uniaxial strain in the GaN buffer and AlN nucleation layers are tensile in nature and arise from the CTE mismatch with the much thicker Si substrate. The measured ε_{zz} strain for the III-nitride layers is compressive, as opposed to the in-plane strain.

The hydrostatic and biaxial strains are calculated using eqs 3, 4, and 7 and are shown in Table 2. The measured hydrostatic strains, ε_h , for all III-nitride layers are <0.1% and relatively small when compared with the measured biaxial strain. Therefore, the primary strain components are biaxial from the measurements.

Using the analytical approach reported by Siddique et al.,⁴² the piezoelectric and spontaneous polarization for the AlGaN barrier ($P_{PE(Barrier)}$, $P_{SP(Barrier)}$, respectively) and GaN buffer layer ($P_{SP(GaN)}$) have been calculated from the XRD determined parameters given in Table 2. A 3% change in the barrier layer biaxial strain state is observed before and after diamond growth. Specifically, the piezoelectric polarization before diamond growth is $P_{PE(Barrier)} = -0.00945 \text{ C/m}^2$, whereas post-diamond growth, it is $P_{PE(Barrier)} = -0.00906 \text{ C/m}^2$. Finally, the 2DEG sheet charge density, N_s , was calculated. The total 2DEG sheet charge density before diamond deposition is $1.04E13 \text{ cm}^{-2}$, whereas the sheet charge density after diamond deposition is $0.99E13 \text{ cm}^{-2}$, which represents a modest 4.5% reduction. These 2DEG sheet charge density values are very comparable⁴² and even higher⁴³ than previously reported values for similar structures and growth conditions.

To check the confidence of the measured parameters, uncertainty analysis was performed considering the different

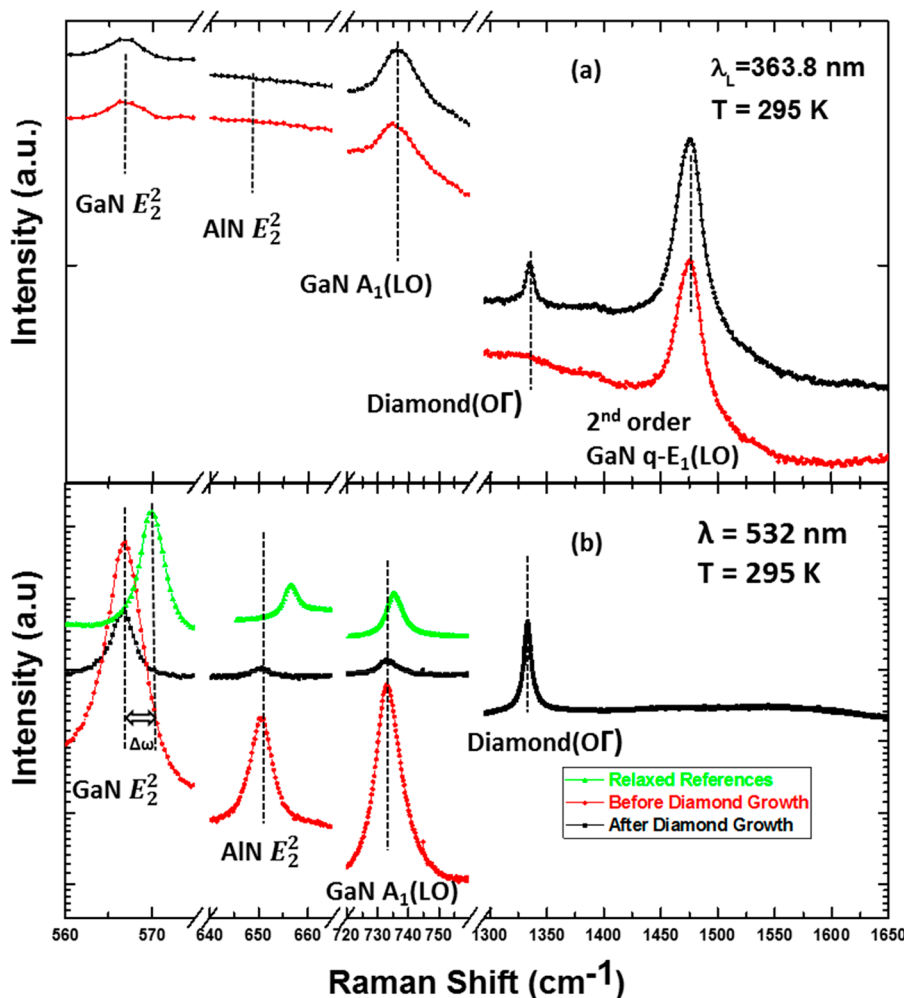


Figure 6. Ultraviolet (a) and visible (b) Raman spectra of the AlGaN/GaN HEMT taken before and after diamond growth. Detail spectra of E_2^2 (GaN, AlN) and A_1 (LO) (GaN) showing phonon red-shift.

sources of uncertainty while determining the RSM peak positions. For the SmartLab Rigaku system with optical precision ≤ 4 arcsec, the instrumental contribution to the uncertainty in determining 2-theta position (and interplanar spacing) is negligible; however, uncertainty arises from the step size in ω -space (0.03°). The maximum uncertainty is estimated using the half-width half-maximum (HWHM) of the GaN buffer layer peaks (prior to diamond deposition) in reciprocal space. First, for biaxial strain, the biaxial stress uncertainty is 0.0003 GPa, or 0.05% of the determined 0.58 GPa value. On the other hand, the uncertainty for determining hydrostatic strain is $8\times$ its calculated value, again, based on the HWHM. Because the hydrostatic strain component is small ($<0.1\%$, discussed previously), we conclude that the measurement uncertainty is insignificant.

The uncertainty resulting from the empirical values of the elastic constants (C_{11} , C_{12} , C_{13} , C_{13}) was also considered. Published elastic constants used here vary up to 19% as reported in the literature by Vurgaftman et al.³⁷ and by Wright et al.,⁴⁴ and shown in Table 1. This results in a biaxial stress uncertainty of ± 0.07 GPa, which is 10% of the determined GaN (post-diamond growth) biaxial stress value of 0.72 GPa, given in Table 2. From this analysis and using the worst-case uncertainty based on the elastic constants, the change in biaxial tensile stress before (0.58 ± 0.05 GPa) to after (0.72 ± 0.07

GPa) diamond deposition is outside the bounds of the experimental uncertainty. Thus, we conclude that there is an increase in the stress due to diamond deposition. Nevertheless, this increase in stress is still significantly below the critical tensile stress (>20 GPa) for material deformation.⁴⁵

3.2. Micro-Raman Results. Figure 6 shows UV (a) and visible (b) micro-Raman spectra for the HEMT stack prior to and following the diamond growth. As a result of the shallow optical penetration depth (≤ 100 nm) in the GaN,²⁴ the UV spectra exhibit scattering from the thick buffer layer only. Observed are E_2^2 and A_1 (LO) symmetry phonons along with a second-order quasi- E_1 (LO) band⁴⁶ at 1476.2 cm^{-1} . Scattering from the GaN layer is strong when using 363.8 nm excitation because of resonance with the direct band gap. The high background in the UV spectra arises from GaN photoluminescence (PL). Post diamond deposition, we see the characteristic $O(\Gamma)$ symmetry phonon at 1332 cm^{-1} and, because diamond is transparent at this wavelength, the GaN buffer layer. This diamond peak appears relatively weak due to the strong resonance with the GaN. Because the III-nitride layers and diamond are transparent to visible light, Raman spectra obtained with this excitation allow the entire material stack to be probed. Consequently, these measurements provide an average property throughout the individual layers. The visible micro-Raman spectra are presented in Figure 6(b); we

Table 3. Peak Positions from Micro-Raman Spectroscopy before and after Diamond Growth^a

parameters	before diamond growth		after diamond growth		
	peak position (cm ⁻¹)	relative shift (cm ⁻¹)	peak position (cm ⁻¹)	relative shift (cm ⁻¹)	
visible Raman spectroscopy	GaN E_2^2 (fwhm) (cm ⁻¹)	566.8 ± 0.1 (3 ± 0.1)	-3.2 ± 0.1	566.6 ± 0.1 (3.4 ± 0.5)	-3.4 ± 0.1
	GaN A_1 (LO) (fwhm)	733.3 ± 0.1 (6.4 ± 0.1)	-2.3 ± 0.2	733.6 ± 0.1 (5.9 ± 0.1)	-1.9 ± 0.1
	AlN E_2^2 (fwhm)	650.6 ± 0.1 (4.1 ± 0.2)	-6.0 ± 0.1	650.8 ± 0.1 (3.2 ± 0.3)	-5.9 ± 0.1
	diamond O(Γ) (fwhm)			1333.2 ± 0.1 (6.4 ± 0.1)	
UV Raman spectroscopy	GaN E_2^2 (fwhm)	566.8 ± 0.1 (4.3 ± 0.1)	-3.3 ± 0.1	566.6 ± 0.1 (4.1 ± 0.2)	-3.4 ± 0.1
	GaN A_1 (LO) (fwhm)	736.1 ± 0.1 (14.0 ± 0.1)	-1.4 ± 0.2	736.4 ± 0.1 (13.3 ± 0.3)	-1.1 ± 0.2
	diamond O(Γ) (fwhm)			1333.2 ± 0.1 (7.3 ± 0.1)	
	second-order quasi- E_1 (LO)	1474.8 ± 0.1 (20.4 ± 0.2)		1475.1 ± 0.1 (20.3 ± 0.1)	

^aBefore and after comparisons are from spatially similar sample locations. The variation obtained by measuring at different positions on the samples ranges from 0.1 to 0.3 cm⁻¹ for visible and UV measurements, respectively. The measured reference values for GaN phonon energies are 570.0 ± 0.1 cm⁻¹ for E_2^2 and 737.6 ± 0.1 cm⁻¹ for A_1 (LO). For the AlN reference, the measured value is 656.7 ± 0.1 cm⁻¹ for E_2^2 .

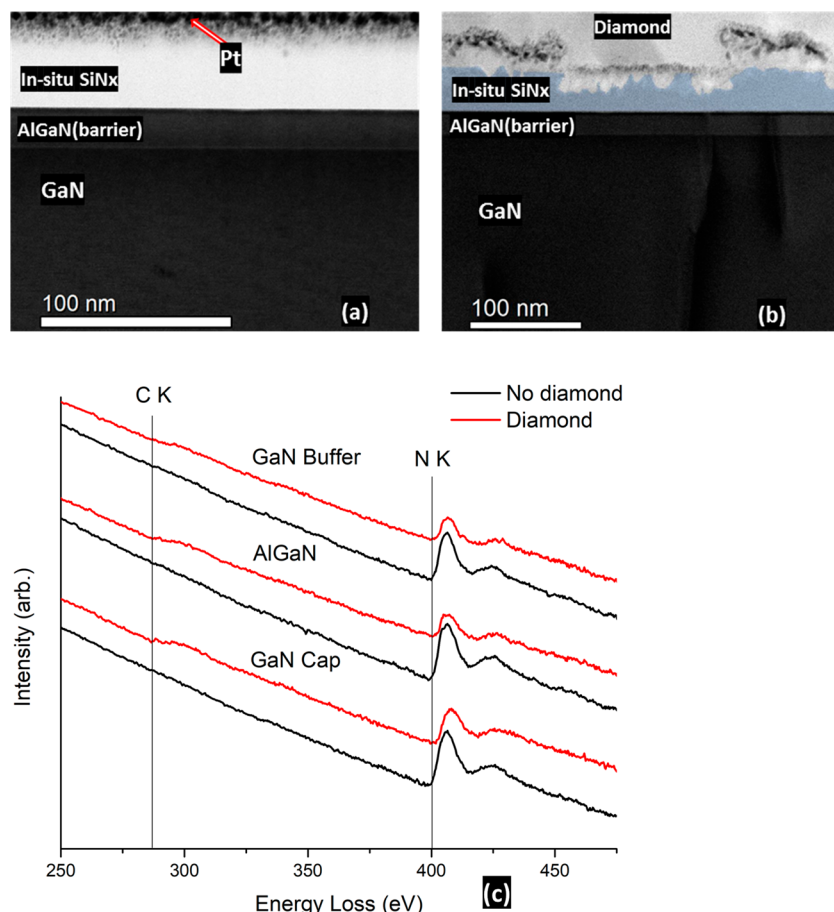


Figure 7. Bright-field STEM images showing the Al(Ga)N/SiNx layer interfacial region (a) before and (b) after diamond growth. (c) EELS comparison point scans with extended collection times.

observe GaN E_2^2 and A_1 (LO) phonons, the AlN E_2^2 band, and, post diamond deposition, the associated O(Γ) line.

The E_2^2 peak positions in GaN and AlN layers are sensitive to stress, whereas the A_1 (LO) position and width are also sensitive to free-carrier concentration. Peak positions and line widths were determined by fitting the data using the Lorentzian function. Results are summarized in Table 3. For the E_2^2 peak position and shift relative to our measured bulk values for GaN and AlN, we determine red-shift in each case corresponding to biaxial tensile stress.¹¹ This agrees with the XRD results and, as discussed above, is primarily attributed to CTE mismatches for each layer and the much thicker Si

substrate. Shifts in the GaN E_2^2 peak positions, relative to the reference material, are consistent in the visible and UV measurements. This consistency applies to the pre- and post-diamond growth comparison. Similarly, the AlN E_2^2 band in the visible Raman spectra is consistent pre- and post-diamond growth. Stress estimates from the Raman measurements may be obtained from the E_2^2 peak shifts using published stress factors,^{38,47,48} which vary between reports for both GaN and AlN. For comparing with the XRD stress values presented in Table 2, we use the Raman-stress factor 4.2 ± 0.3 cm⁻¹/GPa of Kisielowski et al.³⁸ From the visible Raman, we obtain stress values of 0.76 ± 0.06 GPa prior to diamond growth, which is

close to being within the total error of the XRD result for $\sigma_{\text{bs}} = 0.58 \pm 0.07 \text{ GPa}$. Following diamond growth, stress estimated from the Raman measurement is $0.80 \pm 0.06 \text{ GPa}$, which is within the total error of the XRD value of $\sigma_{\text{bs}} = 0.72 \pm 0.07 \text{ GPa}$. Similarly, the stress estimated for AlN depends strongly on the Raman-stress factor and ranges from 1.36 ± 0.32 to $0.95 \pm 0.22 \text{ GPa}$.⁴⁸ These are slightly lower than the XRD values presented in Table 2. Discrepancies in the reported stress factors and elastic coefficients may be attributable to differences in defect densities in the III-nitride layers investigated by the respective teams, which has an impact on the strain values, particularly ε_h , and the Poisson ratio.^{38,49} The primary conclusion from the Raman E_2^2 measurements is consistency seen in values obtained from the GaN and AlN layers prior to and following the growth of the in situ SiN_x and diamond layers.

Shifts measured for the A_1 (*LO*) phonon from GaN are also reported in Table 3. Results obtained using visible Raman scattering are different for the A_1 (*LO*) and E_2^2 phonons. Because the A_1 (*LO*) shifts at a rate of $\sim 2/3$ that of the E_2^2 , based on reported Raman-stress factors for these two phonons,⁵⁰ the observed shifts from the visible measurements are attributable to average stress in the GaN layer. In the UV measurements, however, the shift observed for the A_1 (*LO*) phonon is smaller than what is expected from stress. We tentatively attribute this to the photoinduced free-carrier concentration estimated to be $n = (0.76 \pm 0.31) \times 10^{17} \text{ cm}^{-3}$ based on the empirical formula of Hiroshi et al.⁵¹

3.3. Interface Analysis by STEM. Although the impact of CVD diamond integration on the structural and material properties of the AlGaN layers have been investigated through HRXRD and micro-Raman measurements, it is also important to examine the interface properties. To do so, we conducted cross-sectional STEM measurements before and after diamond growth. The bright-field STEM images in Figure 7(a,b) both show an abrupt interface between the in situ SiN_x and AlGaN barrier layer. A continuous SiN_x layer is critical for effective passivation of state-of-the-art AlGaN/GaN HEMTs.⁵² However, minimizing the thickness of the SiN_x layer is highly beneficial for heat transport from the 2DEG channel to the diamond.^{53,54} We identified a 45 nm in situ SiN_x passivation–adhesion layer as the ideal compromise for these diamond growth conditions.⁵⁵ In particular, the selective thermochemical etching/degredation of the SiN_x , shown in Figure 7(b), must be considered. The initial 45 nm SiN_x layer, while thinned to 20 nm in some regions, remains continuous across the entirety of the AlGaN barrier layer. The AlGaN barrier layer thickness is seen to be unaffected by the diamond deposition as indicated by the consistent 20 nm thickness after diamond growth and in agreement with XRR. Additionally, Figure 7(b) shows a dark contrast region above the SiN_x layer that is due to nanometer scale material from the filament depositing at the initial stage of diamond deposition. This filament material is known to occur in HFCVD diamond,⁵⁶ and the details of this phenomena will be discussed in a separate report.

Carbon diffusion during the CVD diamond deposition process into the GaN buffer layer can be detrimental to device performance and may result in severe current collapse.⁵⁷ To evaluate carbon diffusion, TEM–EELS analysis was chosen because of its higher sensitivity to light elements compared to EDS⁵⁸ and also to avoid issues with secondary X-ray fluorescence from the nearby diamond, which could give

inaccurate results. Typical area mapping does not indicate carbon diffusion into the AlGaN/GaN layers. However, EELS point scans with extended collection times, shown in Figure 7(c), were able to detect trace amounts of carbon, albeit near the detectable limit (generally accepted to be $\sim 0.1\%$ for EELS), in the GaN cap and AlGaN barrier, while the GaN buffer layer exhibits no carbon signal, which is identical to the EELS point scan taken from the wafer before diamond deposition.

3.4. Thermal Characterization by TDTR. Determination of the diamond thermal conductivity and the diamond/GaN TBR was carried out using TDTR. Briefly, TDTR is an optical pump–probe method that utilizes an ultrafast laser with a submicron pulse width. Polarizing optics are used to separate the pulses into separate pump and probe paths. The pump beam then periodically heats the sample, while the probe beam provides information about the transient temperature decay at the surface of the sample. More details of the system used in this study can be found in ref 29. As a result of the complexity of the diamond/HEMT structure in this work, the SiN_x , GaN cap, AlGaN, and AlN between the CVD diamond and the GaN buffer layer were treated as a single interface. This allowed for the determination of an effective TBR that includes the aforementioned layers. Additionally, the relatively large surface roughness of the diamond, 92.4 nm RMS, complicates this measurement and contributes to the uncertainty. Previous work has shown TDTR measurements with a diamond surface roughness RMS up to 100 nm;⁵⁹ however, this is not typical for the majority of reported TDTR studies. By simultaneously fitting for the diamond thickness, diamond thermal conductivity, and diamond/GaN TBR, we were able to determine the unknown parameters as well as check the diamond thickness as reported in the growth. The parameters used in the model are given in Table 4.

Table 4. Parameters Used in the TDTR Model^a

material	thickness (nm)	thermal conductivity [W/m·K]	vol. heat capacity [J/m ³ ·K]
Al	$96 \pm 3\%$	$150 \pm 5\%$	$2.43\text{E}6 \pm 2\%$
CVD diamond	fit	fit	$1.73\text{E}6 \pm 5\%$
GaN	$870 \pm 10\%$	$130 \pm 10\%$	$2.64\text{E}6 \pm 5\%$
AlGaN	$800 \pm 10\%$	$25 \pm 10\%$	$3.09\text{E}6 \pm 5\%$
AlN	$426 \pm 10\%$	$1.5 \pm 10\%$	$2.41\text{E}6 \pm 5\%$
Si	semi-inf	$148 \pm 5\%$	$1.66\text{E}6 \pm 5\%$

^aThe TBR between the Al/diamond and the effective TBR between the CVD diamond/GaN are also fit parameters. All other TBRs were held constant at $10 \text{ m}^2\text{K/GW}$.

It has been shown that for thin diamond films the thermal conductivity is anisotropic because of the columnar polycrystalline growth.⁶⁰ Here we make the simplifying assumption of an effective isotropic thermal conductivity. The diamond thickness determined from the fit was $1.46^{+0.09}_{-0.10} \mu\text{m}$, which is in reasonable agreement with what is measured directly by STEM, $1.25^{+0.12}_{-0.12} \mu\text{m}$. For this thickness, the effective isotropic thermal conductivity of the diamond was $176^{+40}_{-35} \text{ W/m·K}$, and the effective TBR of the diamond/GaN interface (including the SiN_x and additional layers) was $52.8^{+5.1}_{-3.2} \text{ m}^2\text{·K/GW}$. It is important to note the significant difference between bulk diamond thermal conductivity and that of thin films. The thermal conductivity of CVD diamond has been shown to be

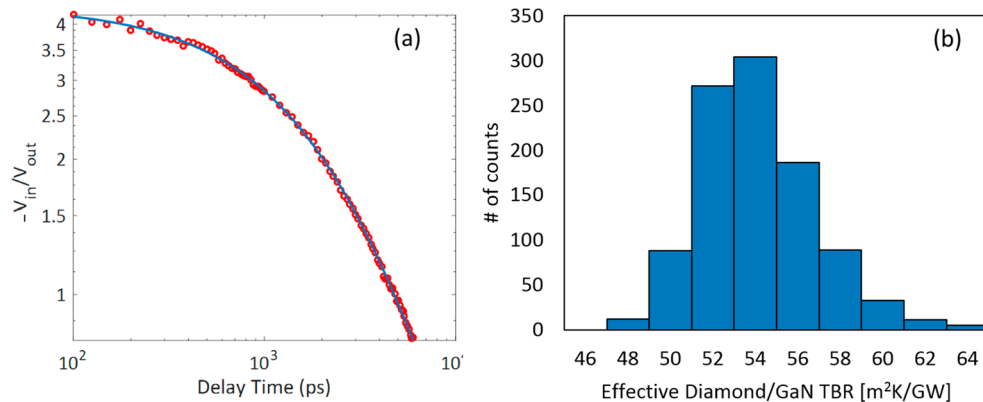


Figure 8. (a) Experimental TDTR data (red circles) and the analytical fit solution (blue line). (b) Normal distribution of the effective diamond/GaN TBR as determined from the Monte Carlo uncertainty. Each fit parameter was estimated by considering the 50th percentile as the measured value, with the 5th and 95th percentiles taken as the lower and upper bounds of uncertainty. The experimental data were subjected to 1000 iterations of the Monte Carlo method in order to obtain the normal distributions.

highly dependent on the thickness of the material because of the nature of the columnar growth structure.²³ For instance, Yates et al. have reported measurements of diamond films ranging from 5 to 13.9 μm , in which the thermal conductivity was shown to vary from 712 to 1362 $\text{W}/\text{m}\cdot\text{K}$ for the respective film thicknesses. Additionally, their work demonstrated the ability to measure a high-quality bulk diamond with a thickness $>300 \mu\text{m}$. In the same work, the impact of boron doping demonstrated thermal conductivity values in a bulk sample of only 650 $\text{W}/\text{m}\cdot\text{K}$, whereas samples with no additional doping were measured to be up to 2200 $\text{W}/\text{m}\cdot\text{K}$.⁶¹ Further work has demonstrated the significantly reduced and nonhomogenous thermal conductivity of 1 μm diamond films by using TDTR to spatially map a suspended membrane. Additionally, a thorough analysis of the implications of using TDTR to measure the thermal conductivity of both diamond films and bulk samples has been undertaken by Bougner et al., where they demonstrated the exceptional capabilities of TDTR as a method to measure the thermal conductivity of such materials.⁶²

Measurement uncertainties were determined using a Monte Carlo method with the 5th and 95th percentiles used as the upper and lower bounds. This method has been previously described in detail²⁹ and consists of assigning each value in the thermal model a relative uncertainty. For each parameter that is not included as a fit parameter, a random distribution of possible values for the nonfit parameters is created based on the assigned uncertainty. The thermal model is then fit to the experimental data multiple times with values for each of the nonfit parameters being randomly varied according to the previously assigned uncertainty. This is performed until convergence on the fit parameters is reached and allows for a normal distribution for each of the fit parameters to be created. In this work, convergence was obtained after 500 iterations; however, 1000 iterations were performed in order to create the normal distributions for each fit parameter. Figure 8 shows the TDTR data fit of the experimental data and the normal distribution of the effective diamond/GaN TBR. The experimental data is fit using a Levenberg–Marquardt algorithm that considers multivariable and nonlinear data fitting. This routine is used to compare the experimentally measured data to a solution for cylindrical radial heat transport through multiple thin films and has been extensively documented in literature.⁶³ The thermal conductivity of the

polycrystalline diamond and TBR values for the diamond/AlGaN/GaN HEMT interface are in the same range (for a $1000 \pm 100 \text{ nm}$ thick diamond, thermal conductivity of 150 to 450 $\text{W}/\text{m}\cdot\text{K}$, and TBR of 50 to 95 $\text{m}^2\text{K}/\text{GW}$) as reported for a similar structure by Zhou et al.²³

The nonfit values used in the thermal model as shown in Table 4 were found in literature and have been consistent with what has been used in previous TDTR models.⁶⁰ The thermal conductivity of the AlGaN was taken from data reported from Lui et al.⁶⁴ In their work, they show no significant variation in thermal conductivity for AlGaN compositions consisting of Al varied between 0.2 and 0.8. This is relevant, because we are considering the two AlGaN layers as a single layer in our model. The AlN thermal properties used in the model were taken from Zhao et al.,⁶⁵ where they measured thin AlN films ranging from 100 to 1050 nm. The value of 1.5 $\text{W}/\text{m}\cdot\text{K}$ is substantially lower than the extrapolated value of 320 $\text{W}/\text{m}\cdot\text{K}$ that was first inferred by Slack et al.⁶⁶ This very large value considered single crystal, defect-free AlN. It has, however, been shown that AlN has a significant size dependence on thermal conductivity.⁶⁷ In addition to a size dependence, the quality of AlN films, which depends on deposition process, grain size, and impurity concentrations, has been shown to have measured variations between 0.4 to 270 $\text{W}/\text{m}\cdot\text{K}$.⁶⁸ In all cases, the thermal conductivity of the AlN in our model is of little consequence to the fit values of the CVD diamond parameters, because the AlN layer is buried below both the GaN and the AlGaN. The use of a pulsed thermal technique such as TDTR will be limited due to the penetration depth of the thermal wave.⁶⁹ In the case of our sample stack, we have no sensitivity to the AlN thermal conductivity regardless if it is 1.5 or 300 $\text{W}/\text{m}\cdot\text{K}$. TDTR sensitivity has been well-documented,⁶² as it considers a fractional change in an independent parameter to the overall change in the reflectance signal. It is clear from Figure 9 that changing the assumed AlN thermal conductivity from 1.5 to 300 $\text{W}/\text{m}\cdot\text{K}$ has no impact on the measurement, whereas the other parameters of interest remain sensitive to the measurement.

4. CONCLUSION

We have investigated the effects of diamond growth on AlGaN/GaN HEMTs when protected by a 46 nm thick in situ SiN_x passivation/adhesion layer. The SiN_x was grown using MOCVD in the same chamber and immediately following the

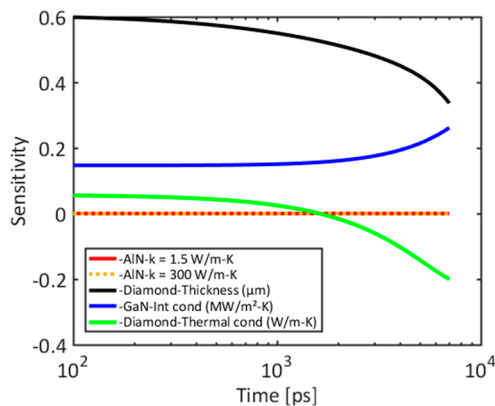


Figure 9. Sensitivity analysis of the TDTR model used in this work. It is clear that the diamond thickness is the most sensitive parameter, and the fit value was found to be in good agreement with the STEM measurements. It is important to point out the lack of sensitivity to the thermal conductivity of the AlN layer. The solid red line indicates an AlN thermal conductivity of 1.5 W/m·K as was used in the model, whereas the dashed orange line is indicative of an AlN thermal conductivity of 300 W/m·K. In both scenarios, we had no sensitivity to this parameter, and it did not impact the other fit parameters of the model.

III-nitride process. The diamond was grown in a hot filament CVD reactor.

Structural integrity and materials properties of the AlGaN/GaN HEMT were evaluated using HRXRD, specifically RSM, and micro-Raman measurements. HRXRD shows a slight increase in the biaxial stress in the GaN layer when comparing pre- (0.58 ± 0.05 GPa) to post- (0.73 ± 0.07 GPa) diamond growth. The RSMs show that the AlGaN barrier layer is unaffected by the diamond deposition. Consistency in the GaN E_2^2 shifts for both visible and UV Raman signifies that the GaN crystal quality is intact and uniform across the thickness before and after the diamond growth.

An abrupt *in situ* SiN_x /AlGaN/GaN interface without any degradation is observed pre- and post-diamond growth. Selective degradation to the *in situ* SiN_x layer at the SiN_x /diamond interface is confirmed using STEM cross-sectional analysis. Even with some selective degradation to the *in situ* SiN_x layer, there is still a >20 nm intact SiN_x to protect the underlying III-nitride layers. Although the degree of degradation to the interface layers depends on the seeding density and diamond growth conditions, in these experiments, for 2% CH_4 and with this seeding method, a 46 nm thick SiN_x passivation/adhesion layer is sufficient to fully protect the AlGaN/GaN HEMT structure during HFCVD diamond growth.

Finally, the thermal conductivity of polycrystalline diamond ($176 + 40/-35$ W/m·K) and the diamond–GaN interface TBR ($52.8 + 5.1/-3.2$ m²·K/GW) values reported here are consistent with those reported for a similar material stack.¹⁸

■ AUTHOR INFORMATION

Corresponding Author

*E-mail: epiner@txstate.edu.

ORCID

Raju Ahmed: [0000-0002-1374-2287](https://orcid.org/0000-0002-1374-2287)

Samuel Graham: [0000-0002-1299-1636](https://orcid.org/0000-0002-1299-1636)

Mark Holtz: [0000-0001-9524-964X](https://orcid.org/0000-0001-9524-964X)

Edwin L. Piner: [0000-0002-5166-4259](https://orcid.org/0000-0002-5166-4259)

Notes

The authors declare no competing financial interest.

■ ACKNOWLEDGMENTS

Funding for this work was provided by the Army Research Office (W911NF-15-1-0424) under the direction of Dr. Joe Qui and by the National Science Foundation (1810419) under the direction of Dr. Dimitris Pavlidis.

■ REFERENCES

- Wu, Y.-F.; Moore, M.; Saxler, A.; Wisleder, T.; Parikh, P. 40-W/Mm Double Field-Plated GaN HEMTs. *2006 64th Device Research Conference 2006*, 151–152.
- El Fatimy, A.; Dyakonova, N.; Meziani, Y.; Otsuji, T.; Knap, W.; Vandenbrouk, S.; Madjour, K.; Théron, D.; Gaquiere, C.; Poisson, M. A.; et al. AlGaN/GaN High Electron Mobility Transistors as a Voltage-Tunable Room Temperature Terahertz Sources. *J. Appl. Phys.* **2010**, *107* (2), 024504.
- Dyakonova, N.; Coquillat, D.; But, D. B.; Teppe, F.; Knap, W.; Faltermeier, P.; Olbrich, P.; Ganichev, S. D.; Szkudlarek, K.; Cywinski, G. Terahertz Detection by AlGaN/GaN HEMTs at High Intensity. *2016 21st International Conference on Microwave, Radar and Wireless Communications (MIKON) 2016*, 1–3.
- Marti, D.; Tirelli, S.; Alt, A. R.; Roberts, J.; Bolognesi, C. R. 150-GHz Cutoff Frequencies and 2-W/Mm Output Power at 40 GHz in a Millimeter-Wave AlGaN/GaN HEMT Technology on Silicon. *IEEE Electron Device Lett.* **2012**, *33* (10), 1372–1374.
- Johnson, J. W.; Piner, E. L.; Vescan, A.; Therrien, R.; Rajagopal, P.; Roberts, J. C.; Brown, J. D.; Singhal, S.; Linthicum, K. J.; Therrien, R.; et al. 12 W/Mm AlGaN-GaN HFETs on Silicon Substrates. *IEEE Electron Device Lett.* **2004**, *25* (7), 459–461.
- Son, K.-A.; Liao, A.; Lung, G.; Gallegos, M.; Hatake, T.; Harris, R. D.; Scheick, L. Z.; Smythe, W. D. GaN-Based High-Temperature and Radiation-Hard Electronics for Harsh Environments. *SPIE Defense, Security, and Sensing 2010*, 7679, 76790U.
- Ambacher, O. Growth and Applications of Group III-nitrides. *J. Phys. D: Appl. Phys.* **1998**, *31* (20), 2653–2710.
- Nazari, M.; Hancock, B. L.; Piner, E. L.; Holtz, M. W. Self-Heating in a GaN-Based Heterojunction Field-Effect Transistor Investigated by Ultraviolet and Visible Micro-Raman Spectroscopy. *2015 IEEE Compd. Semicond. Integr. Circuit Symp. 2015*, *62* (5), 1–4.
- Coe, S.; Sussmann, R. Optical, Thermal and Mechanical Properties of CVD Diamond. *Diamond Relat. Mater.* **2000**, *9* (9–10), 1726–1729.
- Altman, D.; Tyhach, M.; McClymonds, J.; Kim, S.; Graham, S.; Cho, J.; Goodson, K.; Francis, D.; Faili, F.; Ejeckam, F. Analysis and Characterization of Thermal Transport in GaN HEMTs on Diamond Substrates. *2014 IEEE Intersociety Conference on Thermal and Thermomechanical Phenomena in Electronic Systems (ITherm) 2014*, 1199–1205.
- Hancock, B. L.; Nazari, M.; Anderson, J.; Piner, E.; Faili, F.; Oh, S.; Twitchen, D.; Graham, S.; Holtz, M. Ultraviolet Micro-Raman Spectroscopy Stress Mapping of a 75-Mm GaN-on-Diamond Wafer. *Appl. Phys. Lett.* **2016**, *108*, 211901.
- Blevins, J. D.; Via, G. D.; Sutherlin, K.; Tetlak, S.; Poling, B.; Gilbert, R.; Moore, B.; Hoelscher, J.; Stumpff, B.; Bar-Cohen, A. Recent Progress in GaN-on-Diamond Device Technology. *CS MANTECH Conference*, Denver, Colorado, May 19–22, 2014; pp 105–108.
- Sun, H.; Pomeroy, J. W.; Simon, R. B.; Francis, D.; Faili, F.; Twitchen, D. J.; Kuball, M. Temperature-Dependent Thermal Resistance of GaN-on-Diamond HEMT Wafers. *IEEE Electron Device Lett.* **2016**, *37* (5), 621–624.
- Anderson, T. J.; Hobart, K. D.; Tadjer, M. J.; Koehler, A. D.; Imhoff, E. A.; Hite, J. K.; Feygelson, T. I.; Pate, B. B.; Eddy, C. R.; Kub, F. J. Nanocrystalline Diamond Integration with III-Nitride HEMTs. *ECS J. Solid State Sci. Technol.* **2017**, *6* (2), Q3036–Q3039.

(15) Meyer, D. J.; Feygelson, T. I.; Anderson, T. J.; Roussos, J. A.; Tadjer, M. J.; Downey, B. P.; Katzer, D. S.; Pate, B. B.; Ancona, M. G.; Koehler, A. D.; et al. Large-Signal RF Performance of Nanocrystalline Diamond Coated AlGaN/GaN High Electron Mobility Transistors. *IEEE Electron Device Lett.* **2014**, *35* (10), 1013–1015.

(16) Anderson, T. J.; Hobart, K. D.; Tadjer, M. J.; Koehler, A. D.; Feygelson, T. I.; Hite, J. K.; Pate, B. B.; Kub, F. J.; Eddy, C. R. Nanocrystalline Diamond for near Junction Heat Spreading in GaN Power HEMTs. *2013 IEEE Compound Semiconductor Integrated Circuit Symposium (CSICS)* **2013**, 13896029.

(17) Tadjer, M. J.; Anderson, T. J.; Hobart, K. D.; Mastro, M. A.; Hite, J. K.; Caldwell, J. D.; Picard, Y. N.; Kub, F. J.; Eddy, C. R. Electrical and Optical Characterization of AlGaN/GaN HEMTs with in Situ and Ex Situ Deposited SiN x Layers. *J. Electron. Mater.* **2010**, *39* (11), 2452–2458.

(18) Zhou, Y.; Ramaneti, R.; Anaya, J.; Korneychuk, S.; Derluyn, J.; Sun, H.; Pomeroy, J.; Verbeeck, J.; Haenen, K.; Kuball, M. Thermal Characterization of Polycrystalline Diamond Thin Film Heat Spreaders Grown on GaN HEMTs. *Appl. Phys. Lett.* **2017**, *111* (4), 041901.

(19) Babchenko, O.; Vanko, G.; Gerboc, M.; Ižák, T.; Vojs, M.; Lalinský, T.; Kromka, A. Study on Electronic Properties of Diamond/SiNx-Coated AlGaN/GaN High Electron Mobility Transistors Operating up to 500 °C. *Diamond Relat. Mater.* **2018**, *89* (5), 266–272.

(20) Seelmann-Eggebert, M.; Meisen, P.; Schaudel, F.; Koidl, P.; Vescan, A.; Leier, H. Heat-Spreading Diamond Films for GaN-Based High-Power Transistor Devices. *Diamond Relat. Mater.* **2001**, *10* (3–7), 744–749.

(21) Tadjer, M. J.; Anderson, T. J.; Hobart, K. D.; Feygelson, T. I.; Caldwell, J. D.; Eddy, C. R.; Kub, F. J.; Butler, J. E.; Pate, B.; Melngailis, J. Reduced Self-Heating in AlGaN/GaN HEMTs Using Nanocrystalline Diamond Heat-Spreading Films. *IEEE Electron Device Lett.* **2012**, *33* (1), 23–25.

(22) Wang, A.; Tadjer, M. J.; Anderson, T. J.; Baranyai, R.; Pomeroy, J. W.; Feygelson, T. I.; Hobart, K. D.; Pate, B. B.; Calle, F.; Kuball, M. Impact of Intrinsic Stress in Diamond Capping Layers on the Electrical. *IEEE Trans. Electron Devices* **2013**, *60* (10), 3149–3156.

(23) Zhou, Y.; Anaya, J.; Pomeroy, J.; Sun, H.; Gu, X.; Xie, A.; Beam, E.; Becker, M.; Grotjohn, T. A.; Lee, C.; et al. Barrier-Layer Optimization for Enhanced GaN-on-Diamond Device Cooling. *ACS Appl. Mater. Interfaces* **2017**, *9* (39), 34416–34422.

(24) Hancock, B. L.; Nazari, M.; Anderson, J.; Piner, E. L.; Holtz, M. W. Investigation of Stresses in GaN HEMT Layers on a Diamond Substrate Using Micro-Raman Spectroscopy. *2016 IEEE Compound Semiconductor Integrated Circuit Symposium (CSICS)* **2016**, 16499231.

(25) Anderson, T. J.; Hobart, K. D.; Tadjer, M. J.; Koehler, A. D.; Imhoff, E. A.; Hite, J. K.; Feygelson, T. I.; Pate, B. B.; Eddy, C. R.; Kub, F. J. Nanocrystalline Diamond Integration with III-Nitride HEMTs. *ECS J. Solid State Sci. Technol.* **2017**, *6* (2), Q3036–Q3039.

(26) Brown, J. D.; Borges, R.; Piner, E.; Vescan, A.; Singh, S.; Therrien, R. AlGaN/GaN HFETs Fabricated on 100-Mm GaN on Silicon (111) Substrates. *Solid-State Electron.* **2002**, *46* (10), 1535–1539.

(27) Ahmed, R.; Nazari, M.; Hancock, B. L.; Simpson, J.; Engdahl, C.; Piner, E. L.; Holtz, M. W. Ultraviolet Micro-Raman Stress Map of Polycrystalline Diamond Grown Selectively on Silicon Substrates Using Chemical Vapor Deposition. *Appl. Phys. Lett.* **2018**, *112* (18), 181907.

(28) Nazari, M.; Holtz, M. W. Near-Ultraviolet Raman and Micro-Raman Analysis of Electronic Materials. *Appl. Phys. Rev.* **2018**, *5* (4), 041303.

(29) Bouger, T. L.; Yates, L.; Lo, C. F.; Johnson, W.; Graham, S.; Cola, B. A. Thermal Boundary Resistance in GaN Films Measured by Time Domain Thermoreflectance with Robust Monte Carlo Uncertainty Estimation. *Nanoscale Microscale Thermophys. Eng.* **2016**, *20* (1), 22–32.

(30) Huang, H.; Winchester, K. J.; Suvorova, A.; Lawn, B. R.; Liu, Y.; Hu, X. Z.; Dell, J. M.; Faraone, L. Effect of Deposition Conditions on Mechanical Properties of Low-Temperature PECVD Silicon Nitride Films. *Mater. Sci. Eng., A* **2006**, *435*–436, 453–459.

(31) Stoffel, A.; Kovács, A.; Kronast, W.; Müller, B. LPCVD against PECVD for Micromechanical Applications. *J. Micromech. Microeng.* **1996**, *6* (1), 1–13.

(32) Gamarra, P.; Lacam, C.; Tordjman, M.; Medjdoub, F.; di Forte-Poisson, M. A. In-Situ Passivation of Quaternary Barrier InAlGaN/GaN HEMTs. *J. Cryst. Growth* **2017**, *464*, 143–147.

(33) Germain, M.; Cheng, K.; Derluyn, J.; Degroote, S.; Das, J.; Lorenz, A.; Marcon, D.; Van Hove, M.; Leys, M.; Borghs, G. In-Situ Passivation Combined with GaN Buffer Optimization for Extremely Low Current Dispersion and Low Gate Leakage in Si3N4/AlGaN/GaN HEMT Devices on Si (111). *Phys. Status Solidi Curr. Top. Solid State Phys.* **2008**, *5* (6), 2010–2012.

(34) Jana, S. K.; Mukhopadhyay, P.; Ghosh, S.; Kabi, S.; Bag, A.; Kumar, R.; Biswas, D. High-Resolution X-Ray Diffraction Analysis of Al x Ga 1-x N/In x Ga 1-x N/GaN on Sapphire Multilayer Structures: Theoretical, Simulations, and Experimental Observations. *J. Appl. Phys.* **2014**, *115* (17), 174507.

(35) Kadir, A.; Huang, C. C.; Kian Lee, K. E.; Fitzgerald, E. A.; Chua, S. J. Determination of Alloy Composition and Strain in Multiple AlGaN Buffer Layers in GaN/Si System. *Appl. Phys. Lett.* **2014**, *105* (23), 232113.

(36) Denton, A. R.; Ashcroft, N. W. Vegard's Law. *Phys. Rev. A* **1991**, *43* (6), 3161–3164.

(37) Vurgaftman, I.; Meyer, J. R.; Ram-Mohan, L. R. Band Parameters for III-V Compound Semiconductors and Their Alloys. *J. Appl. Phys.* **2001**, *89* (11), 5815–5875.

(38) Kisielowski, C.; Krüger, J.; Ruvimov, S.; Suski, T.; Ager, J.; Jones, E.; Liliental-Weber, Z.; Rubin, M.; Weber, E.; Bremser, M.; et al. Strain-Related Phenomena in GaN Thin Films. *Phys. Rev. B: Condens. Matter Mater. Phys.* **1996**, *54* (24), 17745–17753.

(39) Sewell, R. H.; Musca, C. A.; Dell, J. M.; Faraone, L.; Usher, B. F.; Dieing, T. High-Resolution X-Ray Diffraction Studies of Molecular Beam Epitaxy-Grown HgCdTe Heterostructures and CdZnTe Substrates. *J. Electron. Mater.* **2005**, *34* (6), 795–803.

(40) Harutyunyan, V. S.; Aivazyan, A. P.; Weber, E. R.; Kim, Y.; Park, Y.; Subramanya, S. G. High-Resolution x-Ray Diffraction Strain-Stress Analysis of GaN/Sapphire Heterostructures. *J. Phys. D: Appl. Phys.* **2001**, *34* (10A), A35–A39.

(41) Chowdhury, S.; Biswas, D. Plasma Assisted Molecular Beam Epitaxy Growth and Effect of Varying Buffer Thickness on the Formation of Ultra-Thin In0.17Al0.83N/GaN Heterostructure on Si(111). *Appl. Phys. Lett.* **2015**, *106* (8), 082111.

(42) Siddique, A.; Ahmed, R.; Anderson, J.; Piner, E. L. Effect of Reactant Gas Stoichiometry of In-Situ SiNx Passivation on Structural Properties of MOCVD AlGaN/GaN HEMTs. *J. Cryst. Growth* **2019**, *517* (March), 28–34.

(43) Kudrawiec, R.; Paszkiewicz, B.; Motyka, M.; Misiewicz, J.; Derluyn, J.; Lorenz, A.; Cheng, K.; Das, J.; Germain, M. Contactless Electroreflectance Evidence for Reduction in the Surface Potential Barrier in AlGaN/GaN Heterostructures Passivated by SiN Layer. *J. Appl. Phys.* **2008**, *104* (9), 096108.

(44) Wright, A. F. Elastic Properties of Zinc-Blende and Wurtzite AlN, GaN, and InN. *J. Appl. Phys.* **1997**, *82* (6), 2833–2839.

(45) Umeno, Y.; Kubo, A.; Nagao, S. Density Functional Theory Calculation of Ideal Strength of SiC and GaN: Effect of Multi-Axial Stress. *Comput. Mater. Sci.* **2015**, *109*, 105–110.

(46) Bergman, L.; Dutta, M.; Balkas, C.; Davis, R. F.; Christman, J. A.; Alexson, D.; Nemanich, R. J. Raman Analysis of the E1 and A1 Quasi-Longitudinal Optical and Quasi-Transverse Optical Modes in Wurtzite AlN. *J. Appl. Phys.* **1999**, *85* (7), 3535–3539.

(47) Ahmad, I.; Holtz, M.; Faleev, N. N.; Temkin, H. Dependence of the Stress-Temperature Coefficient on Dislocation Density in Epitaxial GaN Grown on Al_2O_3 and 6H-SiC Substrates. *J. Appl. Phys.* **2004**, *95* (4), 1692–1697.

(48) Prokofyeva, T.; Seon, M.; Vanbuskirk, J.; Holtz, M.; Nikishin, S. A.; Faleev, N. N.; Temkin, H.; Zollner, S. Vibrational Properties of

AlN Grown on (111)-Oriented Silicon. *Phys. Rev. B* **2001**, *63* (12), 125313.

(49) Song, D. Y.; Holtz, M. E.; Chandolu, A.; Bernussi, A.; Nikishin, S. A.; Holtz, M. W.; Gherasoiu, I. Effect of Stress and Free-Carrier Concentration on Photoluminescence in InN. *Appl. Phys. Lett.* **2008**, *92* (12), 121913.

(50) Beechem, T.; Christensen, A.; Green, D. S.; Graham, S. Assessment of Stress Contributions in GaN High Electron Mobility Transistors of Differing Substrates Using Raman Spectroscopy. *J. Appl. Phys.* **2009**, *106* (11), 114509.

(51) Harima, H. Properties of GaN and Related Compounds Studied by Means of Raman Scattering. *J. Phys.: Condens. Matter* **2002**, *14* (38), R967–R993.

(52) Ma, J.; Lu, X.; Zhu, X. L.; Huang, T. D.; Xu, P. Q.; Lau, K. M.; Jiang, H. MOVPE Growth of in Situ SiN x/AlN/GaN MISHEMTs with Low Leakage Current and High on/off Current Ratio. *J. Cryst. Growth* **2015**, *414* (March), 237–242.

(53) Cho, J.; Chu, K. K.; Chao, P. C.; McGraw, C.; Asheghi, M.; Goodson, K. E. Thermal Conduction Normal to Thin Silicon Nitride Films on Diamond and GaN. *Thermomechanical Phenom. Electron. Syst.-Proceedings Intersoc. Conf.* **2014**, 1186–1191.

(54) Sun, H.; Simon, R. B.; Pomeroy, J. W.; Francis, D.; Faili, F.; Twitchen, D. J.; Kuball, M. Reducing GaN-on-Diamond Interfacial Thermal Resistance for High Power Transistor Applications. *Appl. Phys. Lett.* **2015**, *106* (11), 111906.

(55) Ahmed, R.; Siddique, A.; Anderson, J.; Engdahl, C.; Holtz, M.; Piner, E. Selective Area Deposition of Hot Filament CVD Diamond on 100 Mm MOCVD Grown AlGaN/GaN Wafers. *Cryst. Growth Des.* **2019**, *19* (2), 672–677.

(56) Oliphant, C. J.; Arendse, C. J.; Camagu, S. T.; Swart, H. EBSD Analysis of Tungsten-Filament Carburization during the Hot-Wire CVD of Multi-Walled Carbon Nanotubes. *Microsc. Microanal.* **2014**, *20* (1), 4–13.

(57) Klein, P. B.; Binari, S. C.; Ikossi, K.; Wickenden, A. E.; Koleske, D. D.; Henry, R. L. Current Collapse and the Role of Carbon in AlGaN/GaN High Electron Mobility Transistors Grown by Metal-organic Vapor-Phase Epitaxy. *Appl. Phys. Lett.* **2001**, *79* (21), 3527–3529.

(58) Leapman, R. D.; Hunt, J. A. Comparison of Detection Limits for EELS and EDXS. *Microsc., Microanal., Microstruct.* **1991**, *2* (2–3), 231–244.

(59) Gengler, J. J.; Roy, S.; Jones, J. G.; Gord, J. R. Two-Color Time-Domain Thermoreflectance of Various Metal Transducers with an Optical Parametric Oscillator. *Meas. Sci. Technol.* **2012**, *23* (5), 055205.

(60) Yates, L.; Anderson, J.; Gu, X.; Lee, C.; Bai, T.; Mecklenburg, M.; Aoki, T.; Goorsky, M. S.; Kuball, M.; Piner, E. L.; et al. Low Thermal Boundary Resistance Interfaces for GaN-on-Diamond Devices. *ACS Appl. Mater. Interfaces* **2018**, *10* (28), 24302–24309.

(61) Yates, L.; Sood, A.; Cheng, Z.; Bouher, T.; Malcolm, K.; Cho, J.; Asheghi, M.; Goodson, K.; Goorsky, M.; Faili, F.; et al. Characterization of the Thermal Conductivity of CVD Diamond for GaN-on-Diamond Devices. *2016 IEEE Compound Semiconductor Integrated Circuit Symposium (CSICS) 2016*, 16489225.

(62) Bouher, T. L.; Yates, L.; Cheng, Z.; Cola, B. A.; Graham, S.; Chaeito, R.; Sood, A.; Asheghi, M.; Goodson, K. E. Experimental Considerations of CVD Diamond Film Measurements Using Time Domain Thermoreflectance. *2017 16th IEEE Intersociety Conference on Thermal and Thermomechanical Phenomena in Electronic Systems (ITherm) 2017*, 30–38.

(63) Liu, J.; Zhu, J.; Tian, M.; Gu, X.; Schmidt, A.; Yang, R. Simultaneous Measurement of Thermal Conductivity and Heat Capacity of Bulk and Thin Film Materials Using Frequency-Dependent Transient Thermoreflectance Method. *Rev. Sci. Instrum.* **2013**, *84* (3), 034902.

(64) Liu, W.; Balandin, A. A. Temperature Dependence of Thermal Conductivity of Al XGa 1-x Thin Films Measured by the Differential 3ω Technique. *Appl. Phys. Lett.* **2004**, *85* (22), 5230–5232.

(65) Zhao, Y.; Zhu, C.; Wang, S.; Tian, J. Z.; Yang, D. J.; Chen, C. K.; Cheng, H.; Hing, P. Pulsed Photothermal Reflectance Measurement of the Thermal Conductivity of Sputtered Aluminum Nitride Thin Films. *J. Appl. Phys.* **2004**, *96* (8), 4563–4568.

(66) Slack, G. A. Nonmetallic Crystals with High Thermal Conductivity. *J. Phys. Chem. Solids* **1973**, *34* (2), 321–335.

(67) Freedman, J. P.; Leach, J. H.; Preble, E. A.; Sitar, Z.; Davis, R. F.; Malen, J. A. Universal Phonon Mean Free Path Spectra in Crystalline Semiconductors at High Temperature. *Sci. Rep.* **2013**, *3*, 2963.

(68) Watari, K.; Shinde, S. L. High Thermal Conductivity Materials. *MRS Bull.* **2001**, *26* (06), 440–444.

(69) Braun, J. L.; Hopkins, P. E. Upper Limit to the Thermal Penetration Depth during Modulated Heating of Multilayer Thin Films with Pulsed and Continuous Wave Lasers: A Numerical Study. *J. Appl. Phys.* **2017**, *121* (17), 175107.